

# Successful integration of CFD and experiments in fluid dynamics: the computational investigator point of view

G. Degrez<sup>1,2</sup> W. Dieudonné<sup>1</sup> & T. Magin<sup>1,2</sup>

1 von Karman Institute for Fluid Dynamics, Belgium,  
corresponding author, gdegrez@ulb.ac.be

2 Fluid mechanics laboratory, Université Libre de Bruxelles, Belgium

## Abstract

## Introduction

The tremendous development of numerical simulation in science and engineering over the past 30 to 40 years has brought a revolution in the scientific research and engineering practise. This is in particular true in aerodynamics where CFD is now ubiquitous in research and design. The development of computational tools and capabilities (computer hardware, computational algorithms, physical models) has however been so fast that the scientific and engineering community hasn't developed the complete expertise of the appropriate use of these simulation tools yet.

A fundamental question in this respect is that of the reliability of numerical simulations. This question has received an increasing attention over the past few years and has prompted a blossoming of verification and validation activities [1, 2] and the elaboration of verification and validation standards [3]. Validation activities are certainly one of the applications which requires a close integration of the CFD simulations and experiments. Requirements from experiments for validation activities will be illustrated by a sample study carried out at VKI a few years back [4].

About 10 years ago, VKI started the design and construction of a large inductively coupled plasma wind tunnel to be used for testing of thermal protection systems materials. As a result, it got involved in high enthalpy flow research, which is an area where, because of the difficulty in performing experimental measurements and the complexity of the physico-chemical models inserted in the CFD models, a close integration of CFD simulations and experiments is also needed. Two examples of high enthalpy flow studies combining CFD and experiments will be presented and discussed, with emphasis on the requirements from experiments.

## Validation study – Hypersonic flow over a blunted cone-flare

The hypersonic flow over a blunted cone-flare was selected as a unit problem (according to the terminology proposed by Oberkampf [5]) for the validation of CFD solvers for reentry flow problems, because it possesses some of the major features of flows over reentry vehicles. Because of the blunt geometry, a bow shock wave is formed with the associated entropy layer, and the flare induces flow separation and recirculation. Also, to reduce computational complexity and allow a more thorough grid refinement study, attention was restricted to the axisymmetric zero angle of attack configuration.

A first requirement from the experiment was thus to make sure that the flow was really axisymmetric (or, almost equivalently, that the angle of attack was really zero). This was very carefully checked by the experimental investigators through surface pressure and heat transfer measurements. Model pitch and yaw were adjusted until the surface pressure and heat transfer distributions were truly axisymmetric. This is illustrated in Fig. 1 which shows pressure distribu-

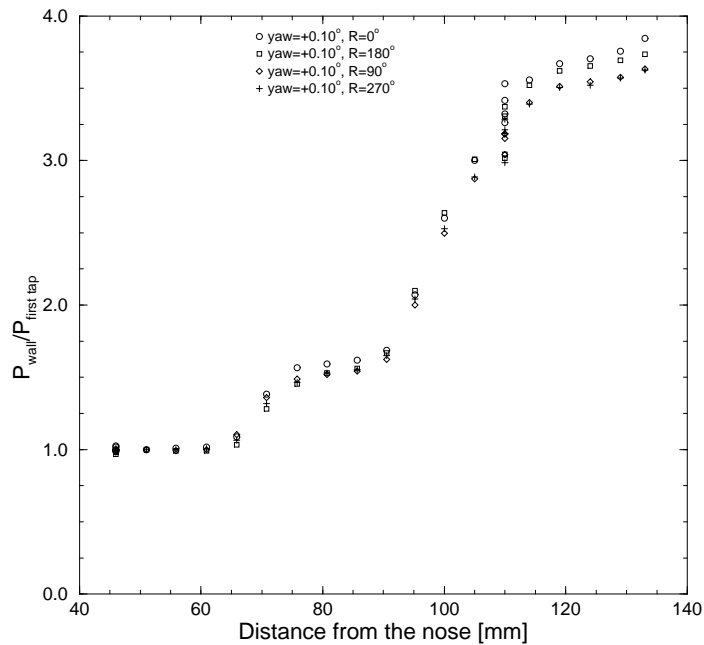


Figure 1: Pressure distributions for 4 azimuthal positions

tions along 4 meridian lines (obtained by rotating the model 0, 90, 180 and 270° around its axis). The flow was found extremely sensitive to model misalignment, with significant differences in flow data being observed for an angle of attack as small as 0.1°, as illustrated in Fig. 2 which shows temperature contours for a 0.25° yaw angle.

The repeatability and uncertainties of experimental measurements were carefully assessed, as illustrated by the surface pressure distributions shown in Fig. 3. The uncertainties on surface pressure and heat transfer coefficient (Stanton number) were estimated to be  $\pm 7\%$  and  $\pm 11.5\%$

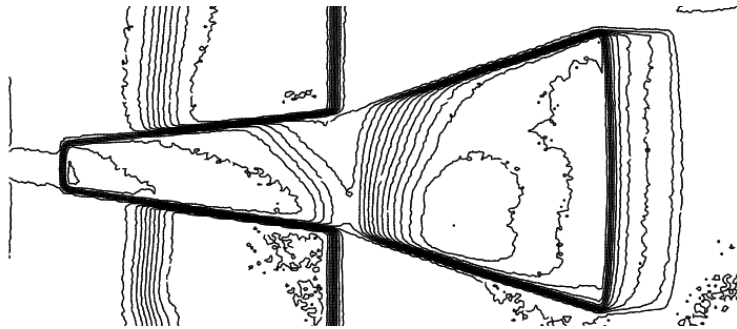


Figure 2: Effect of yaw (0.25°) on IR thermogram

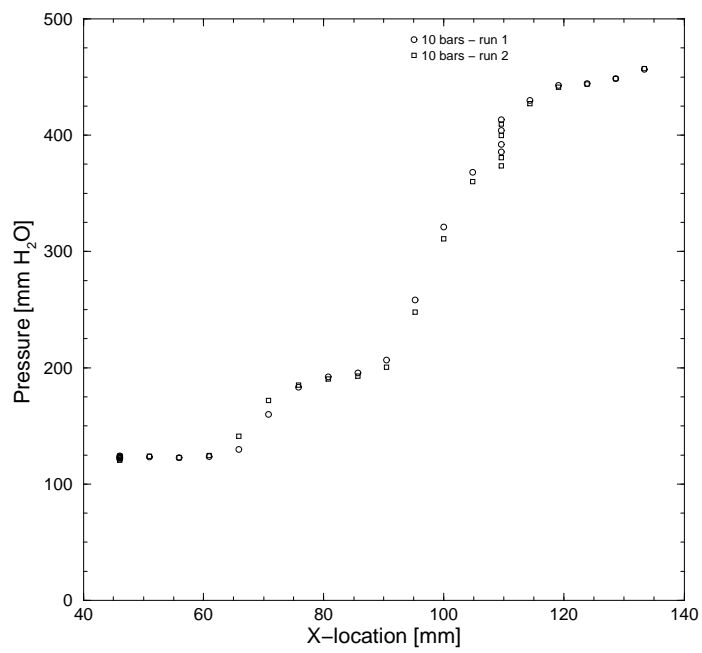


Figure 3: Repeatability of consecutive runs

respectively.

The computational study was performed using a multiblock cell-centered finite volume flow solver developed at VKI [6, 7], which features a variety of upwind flux functions, and limiters. All computations were performed using the hybrid upwind flux of Coquel & Liou [8]. Grids were generated using a hyperbolic grid generator developed at VKI. A fine grid was generated, from which coarser grids were derived by eliminating every other grid line. Solutions were obtained using a grid sequencing technique (also called one-way multigrid), i.e. calculating first the solution the coarsest mesh, then using the converged solution as an initial guess on the next grid level, until the finest grid. Three grids were used, a fine grid with  $400 \times 80$  interior cells ( $401 \times 81$  grid lines), a medium grid with  $200 \times 40$  interior cells, and a coarse grid with  $100 \times 20$  interior cells.

The computational solution on the finest grid is shown on Fig. 4, for an incoming uniform flow at  $M_\infty = 6.00$ ,  $p^0 = 1,064$  MPa, and  $T^0 = 550$  K. One clearly observes the bow shock, as well as the separation and reattachment shocks, and the low Mach number (recirculation) region around the flare hinge line. Comparisons of the surface pressure and heat transfer distributions

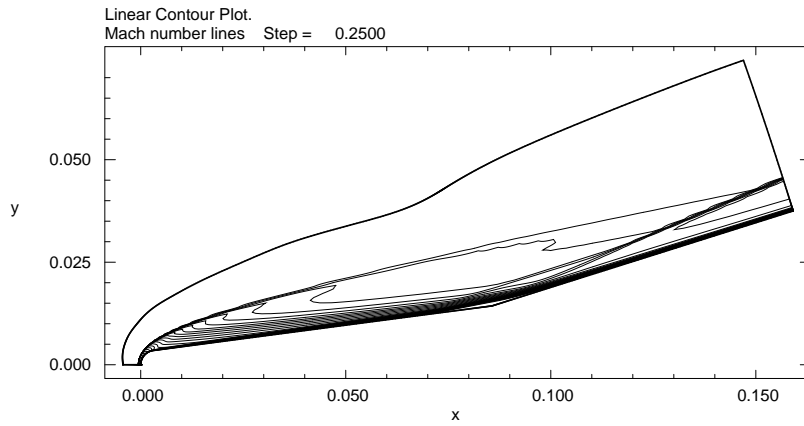


Figure 4: Computed Mach number contours

on the three grids are shown on Figs. 5–6. Although the pressure and Stanton number distributions on the cone appear to be grid-converged on the medium and fine grids, the solution is clearly not grid-converged in the separated region, the size of which significantly increases between the medium and fine grids. This is best shown by the separation and reattachment point locations on the three grids.

Grid	coarse	medium	fine
$x_{\text{sep}}/x_{\text{hinge}}$	0.9496	0.8939	0.8579
$x_{\text{reat}}/x_{\text{hinge}}$	1.0491	1.1059	1.1428

Table 1: Separation and reattachment point locations

The fine grid computational results are compared to the experimental results on Figs. 7–8. Agreement of the pressure distributions upstream of the separation point is seen to be excellent, but the size of the computed separated region is seen to be smaller than the experimental one, which confirms that the computed solutions are not grid-converged in the separated region.

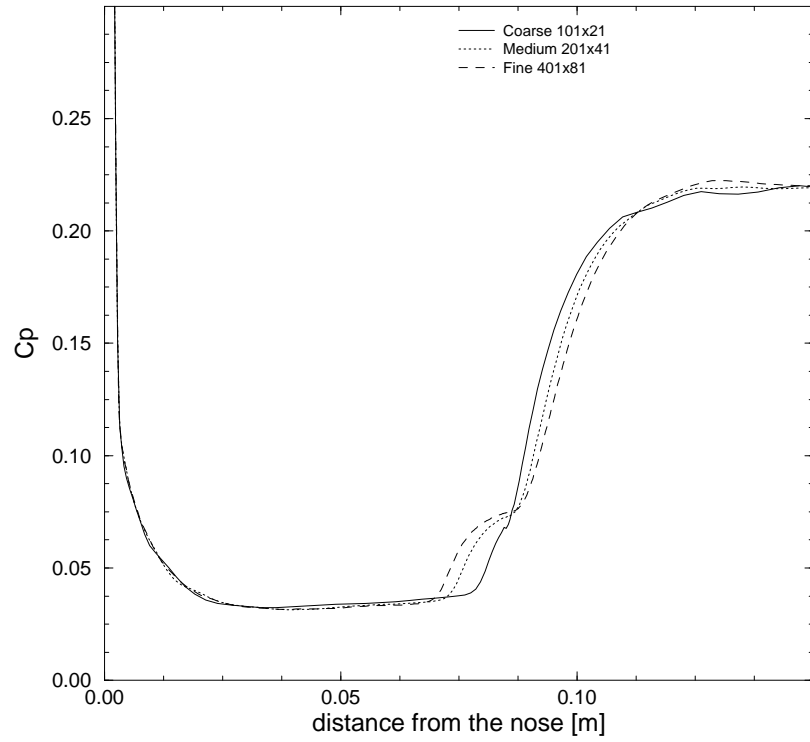


Figure 5: Computed pressure coefficient distribution

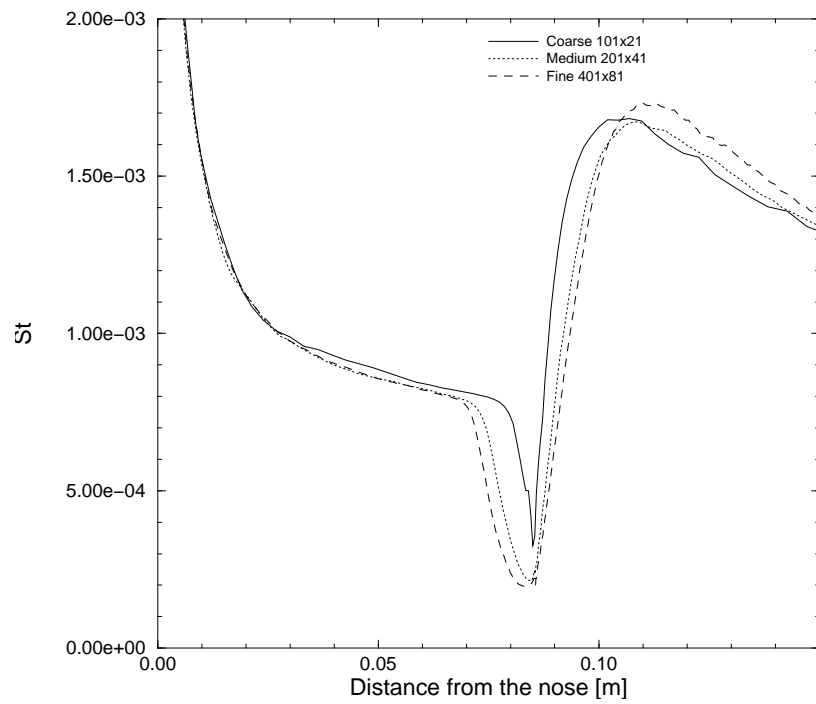


Figure 6: Computed Stanton number distribution

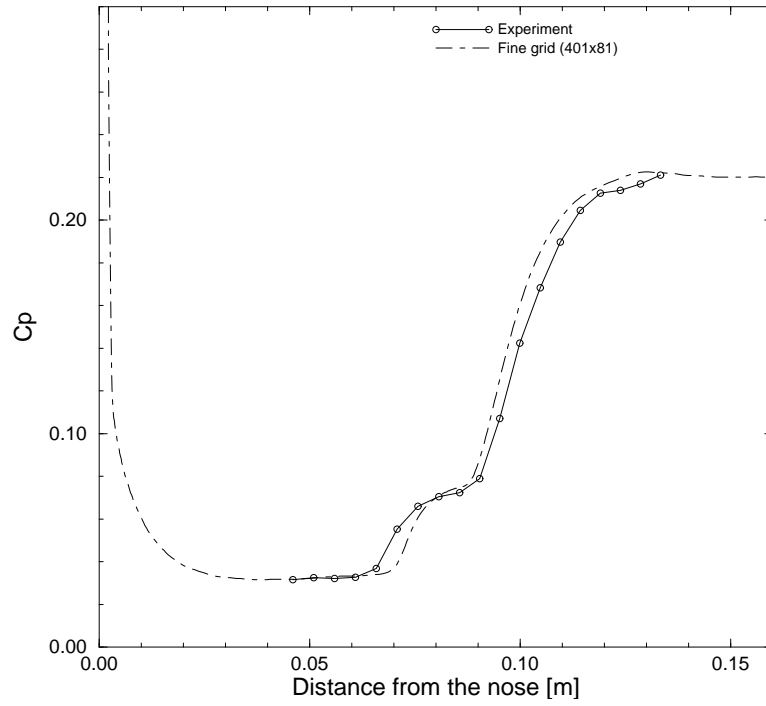


Figure 7: pressure coefficient distributions

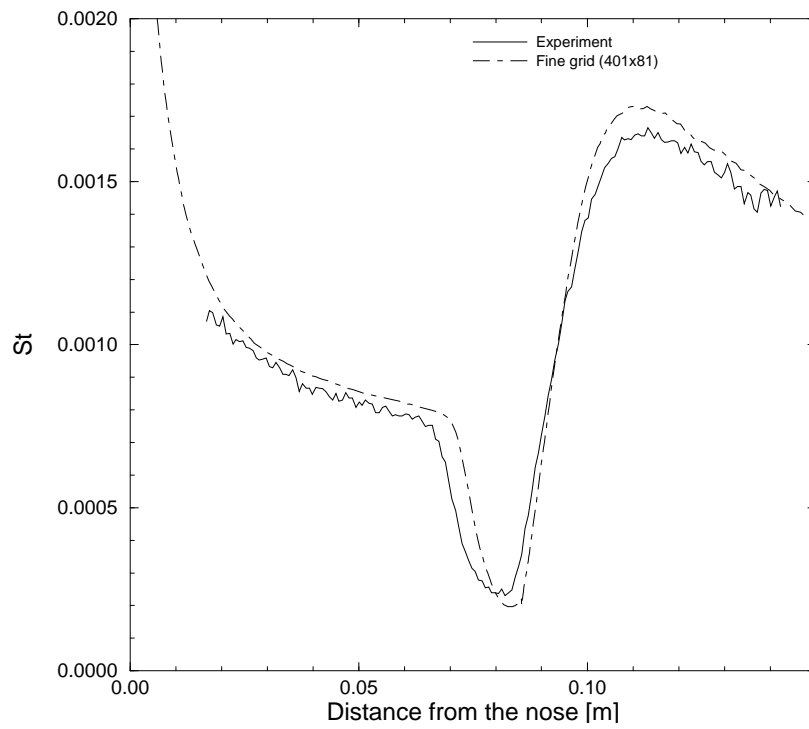


Figure 8: Stanton number distributions

Similar observations are made on the heat transfer distributions, but in addition, there appears to be an offset of about 4% in the Stanton number on the cone upstream of the separated region. Although this is within the experimental uncertainty, it appears to be a systematic error (bias) rather than a random (stochastic) error.

The origin of this systematic error was then investigated. It was suspected that the assumption of a uniform incoming flow at Mach 6 might not be valid. Facility calibration experiments have indeed revealed [9] that there were some (relatively small) non-uniformities in the test section flow properties: the flow is virtually axisymmetric, but there are some radial and axial gradients, in particular an axial acceleration. However, the facility calibration data were not sufficiently detailed to be used as boundary conditions for the numerical computation. This illustrates another requirement from experiments: that they provide a complete set of boundary and initial conditions data [5]. This is unfortunately very rarely the case, because of either the difficulty or the cost of collecting these data. To circumvent this difficulty, it was decided to rebuild the test section flow conditions numerically. The flow in the H3 wind tunnel nozzle and in the free jet downstream of the nozzle was computed with the same flow solver (computational domain shown on Fig. 9). There is however a major difference with the blunted cone-flare



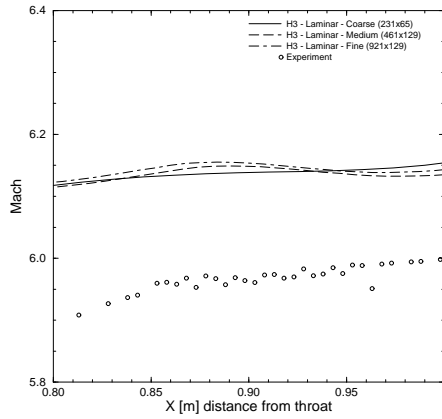
Figure 9: H3 nozzle geometry

problem, namely that the nozzle wall boundary layer undergoes transition at some point along the wall, the transition location being unknown. The numerical rebuilding strategy was then to vary the transition point location in the computational simulation until a good match was found with experimental pitot pressure surveys in the free jet downstream of the nozzle exit [9]. This is typical example of numerical model calibration as defined in the AIAA guidelines for verification and validation [3]. Computations were performed using the Spalart & Allmaras 1 equation model [10]. Again, a grid sensitivity study was performed using three grids whose characteristics are summarized in Table 2. Computed centerline Mach number distributions

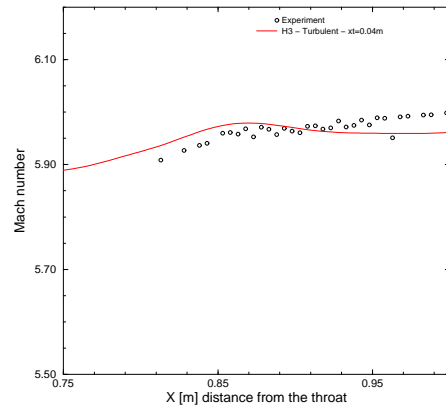
Table 2: Nozzle grids

Grid level	laminar computations			turbulent computations		
	Coarse	Medium	Fine	Coarse	Medium	Fine
nozzle & test section	208 × 33	415 × 65	829 × 129	231 × 33	461 × 65	921 × 129
tunnel chamber	23 × 33	45 × 65	89 × 129	23 × 33	45 × 65	89 × 129

are shown on Fig. 10 for both a fully laminar and a turbulent computation with the transition point location  $x_t$  4 cm downstream of the nozzle throat, together with the experimental results. One observes that the centerline Mach number is overpredicted by the laminar computation. This is explained by the fact that the laminar boundary layer thickness is much smaller than the real one, and as a result, the effective nozzle cross section is larger, and the flow is thus more expanded. On the other hand, there's a good agreement between the turbulent computation



(a) laminar computation



(b) turbulent computation

Figure 10: Centerline Mach number distribution

results (for the selected value of the transition point location) and the experimental data. This is confirmed by the comparison of the computed and experimental pitot pressure profile across the jet shown in Fig. 11.

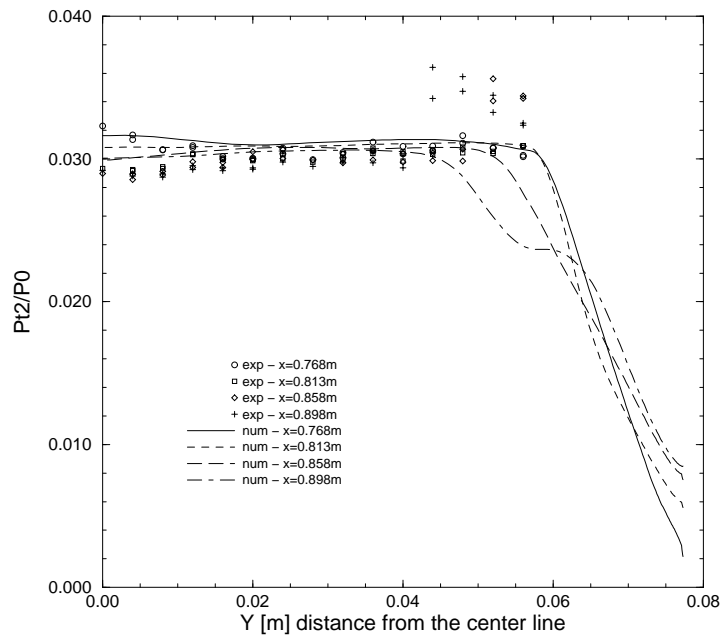


Figure 11: Pitot pressure profiles across jet ( $x_t = 0.04m$ )

The corresponding flowfield is visualized in Fig. 12–14. One observes the formation of a com-

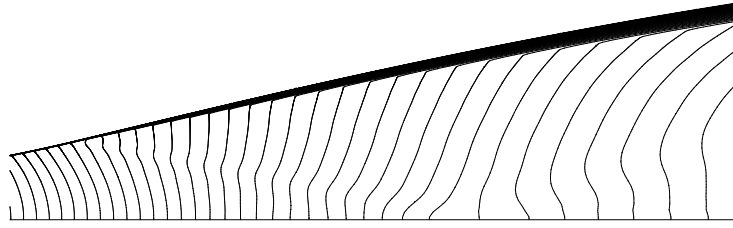


Figure 12: Mach number contours near nozzle throat

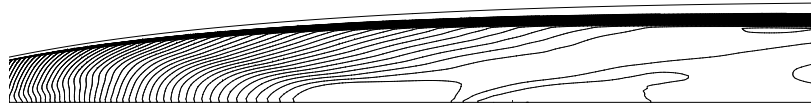


Figure 13: Mach number contours in nozzle



Figure 14: Mach number contours in jet flow

pressure wave slightly downstream of the nozzle throat (Fig. 12) which reflects along the nozzle axis and wall along the whole nozzle (Fig. 13), producing appreciable flow non-uniformities in the nozzle exit section and in the downstream jet (Fig. 14, contours scale emphasizes non-uniformities).

The effect of the test section flow non-uniformities on the blunted cone-flare flow was then investigated by recomputing the flow with inflow boundary conditions obtained from the nozzle/jet flow solution (by interpolation). The flow Mach number distribution on the inflow boundary is displayed on Fig. 15, showing that it is close to 5.9 over the major part of the boundary.

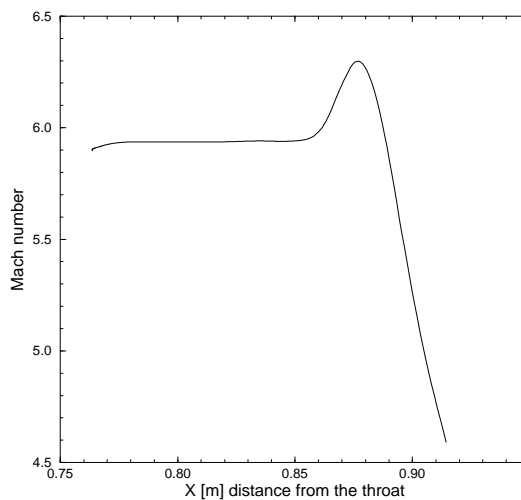


Figure 15: Mach number distribution on inflow boundary

Computations were performed on the three grids again. Fine grid pressure and Stanton number distributions are compared to the experimental results and uniform flow computations on Figs. 16–17. Discrepancies in the separated region due to insufficient grid resolution are of

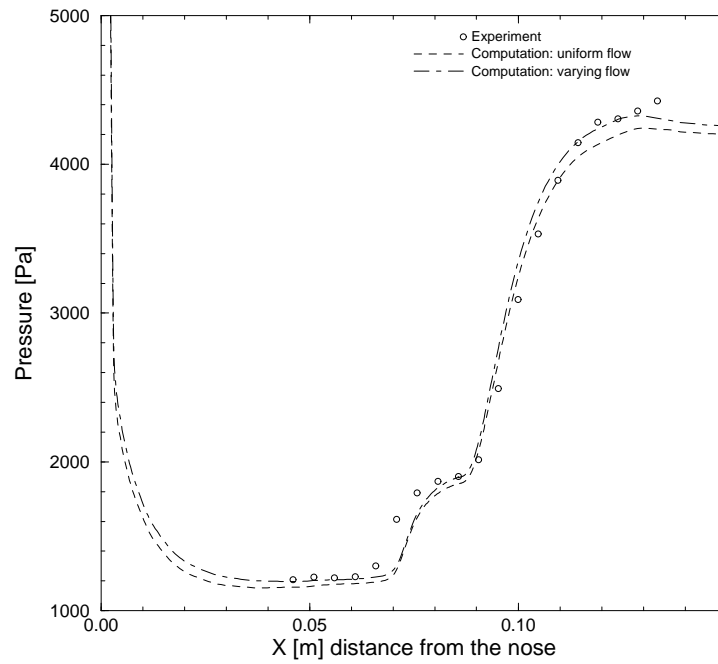


Figure 16: Pressure distributions

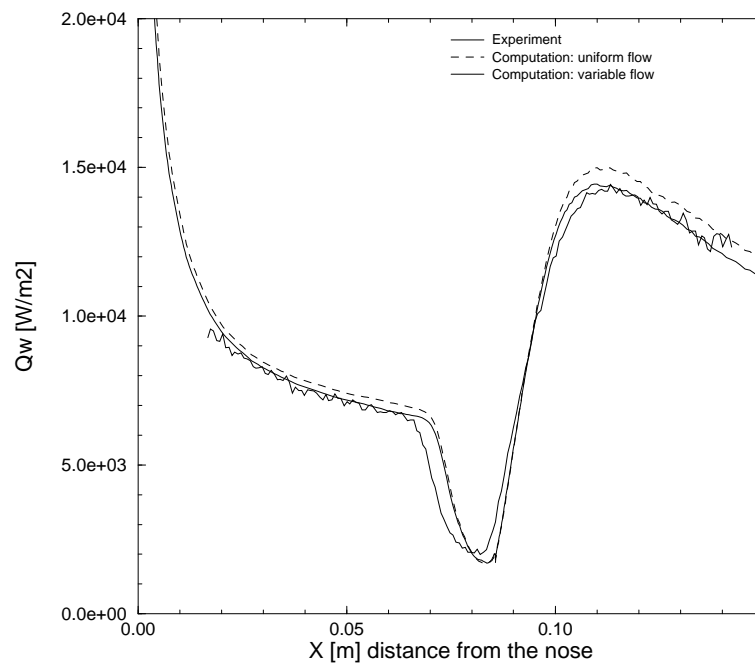


Figure 17: Heat flux distributions

course still present, but the heat transfer on the cone upstream of separation is now in agreement with the experimental data, showing that the offset was indeed due to incorrect inflow boundary conditions. Now, since the flow over the cone-flare comes from a narrow tube around

the tunnel axis, and flow properties in that tube are almost uniform with  $M_\infty = 5.90$ , it was wondered whether a computation with a uniform Mach 5.90 inflow might provide a similarly good agreement with the experiments. This is indeed the case as shown on Fig. 18.

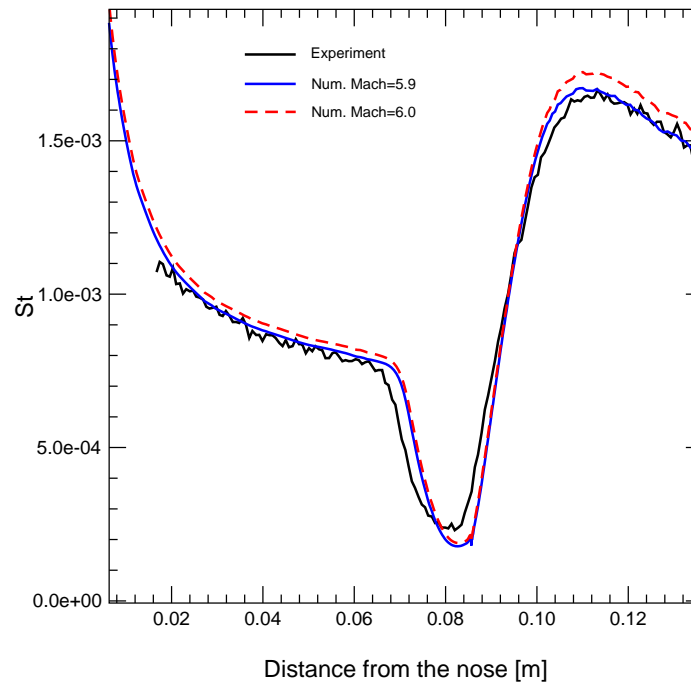


Figure 18: Stanton number distributions, uniform  $M_\infty = 5.90$  inflow

## Flows in inductively coupled plasma (ICP) facilities

### Determination of wall catalytic efficiency by combined experiments and computations

One of the main design parameters for reentry vehicles is the maximum wall heat flux over the reentry trajectory, which controls the size, and thus the weight, of the vehicle thermal protection system (TPS). Now, if the boundary layer developing on the vehicle is far from chemical equilibrium, the wall heat flux strongly depends on the wall catalytic activity, with differences by as much as a factor of two between a non-catalytic and a fully catalytic surface. Until recently, the design of TPS has been made assuming the most unfavourable condition, i.e. a fully catalytic surface. This excessively conservative approach is no longer acceptable for the design of the next generation of reusable space vehicles because of the weight and operative costs it imposes, especially for the longer range missions such as Mars exploration.

Now, in order to take finite catalytic wall activity into account, TPS materials catalytic properties in flow conditions (pressure, temperature, chemical composition) as close as possible to the flight conditions need to be known with a good accuracy. Unfortunately, TPS materials catalytic efficiency in flight conditions cannot be reliably calculated a priori using some physico-chemical theory or computational model, or measured directly, it has to be determined indirectly through its effect on wall heat flux on a TPS material sample in a ground testing facility. This is currently

done at VKI using a methodology combining experiments and computational simulations originally developed by Kolesnikov *et al.* [11, 12] at the Institute for Problems in Mechanics (IPM), Moscow. The principles of the methodology, which is schematically represented in Fig. 19, will

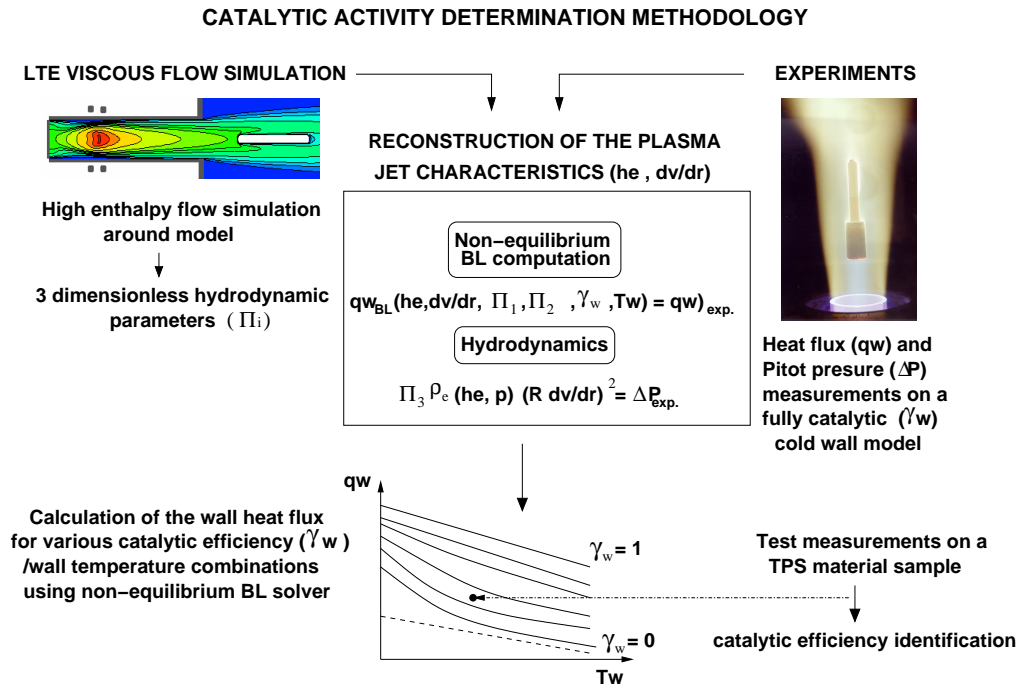


Figure 19: Schematic of IPM methodology for catalytic activity determination

now be explained.

It is well known that, in the vicinity of a stagnation point, the Navier-Stokes equations have a self-similar solution, for variable density as well as constant density flows. This is also true for flows in chemical non-equilibrium, such as around the TPS material sample in the VKI inductively coupled plasma (ICP) facility, and it results from the analysis of the self-similar stagnation line flow equations that the stagnation point heat flux is a function of the following quantities

- the thermodynamic state at the boundary layer edge, which, assuming chemical equilibrium at the boundary layer edge, is completely determined by two variables, e.g.  $p_e$  and  $h_e$ ,
- the radial velocity gradient  $(\partial v / \partial r)_e$  at the boundary layer edge,
- the boundary layer thickness ( $\delta$ ) and the product of the normal (i.e. axial) velocity by the normal derivative of the radial velocity gradient at the boundary layer edge  $(u_e \frac{\partial}{\partial x} (\frac{\partial v}{\partial r})_e)$  — these two parameters are needed because the typically low Reynolds numbers of the flow around the probe impose to take finite boundary layer thickness effects into account —, and
- the wall catalytic activity, represented by a unique recombination probability  $\gamma_w$  and the wall temperature  $T_w$ .

Defining the following non-dimensional parameters

$$\Pi_1 \equiv \frac{\delta}{R} \quad \Pi_2 \equiv u_e \frac{\partial}{\partial x} \left( \frac{\partial v}{\partial r} \right)_e / \left( \frac{\partial v}{\partial r} \right)_e^2, \quad (1)$$

where  $R$  is the TPS material sample radius, the wall heat flux can thus be expressed as

$$q_w = BL(p_e, h_e, \left( \frac{\partial v}{\partial r} \right)_e, \Pi_1, \Pi_2, \gamma_w, T_w) \quad (2)$$

Now, the actual expression of the function is not known analytically, but rather through the application of a one-dimensional computational model [13, 14] which solves the governing set of ODEs using a compact fourth order Hermitian finite difference scheme. Using this model, the recombination probability  $\gamma_w$  can thus be determined if all other quantities are known.

As indicated in Fig. 19, the wall heat flux and the wall temperature are experimentally measured. The other quantities are determined from a combination of computations and experiments. The boundary layer edge properties and velocity gradient clearly depend on the ICP facility operational parameters, i.e. inlet mass flow, pressure level and power injected in the plasma. Inlet mass flow and operating pressure are directly measured, but the power actually injected in the plasma is unknown, and thus needs to be reconstructed.

A computational model of LTE flow in an ICP facility developed at VKI [15, 16] is used for this purpose. It is based on a pressure-stabilized collocated cell-centered finite volume formulation for the flow equations with second order upwind discretization of the convective fluxes, together with a cell-centered finite volume formulation for the 2D (fully resistive) electric field equation. In LTE, it has been shown by the IPM scientists, and confirmed at VKI, that the flow pattern depends almost exclusively on the inlet mass flow, which directly controls the flow Reynolds number. For a given mass flow, solutions at various pressure/power combinations are seen to be similar, as confirmed by the fact that the non-dimensional parameters  $\Pi_{1,2}$  remain constant, independently of the pressure/power combination. These parameters are thus determined by a computational simulation of the LTE flow in the ICP facility.

To reconstruct the unknown power injected in the plasma, or equivalently the boundary layer edge enthalpy and velocity gradient, two auxiliary measurements are performed, namely of the stagnation point heat flux ( $q_w$ ) on a cold wall ( $T_w \sim 300$  to  $400$  K) reference heat flux probe assumed to be fully catalytic, and of the pitot pressure ( $\Delta p$ ) on a cooled pitot probe. In a low speed cold flow at large Reynolds number, a pitot probe essentially measures the local dynamic pressure ( $\Delta p = \rho u^2/2$ ). At low Reynolds numbers, such as those currently encountered in ICP facilities, corrections must be applied to this relation, such as the correlation due to Homann [17], i.e.

$$\frac{2\Delta p}{\rho_e u_e^2} = K_p(Re) = 1 + \frac{6}{Re + 0.455 \sqrt{Re}}. \quad (3)$$

This relation can be rewritten as

$$\frac{2\Delta p}{\rho_e \left( R \left( \frac{\partial v}{\partial r} \right)_e \right)^2} = K_p \left( \frac{u_e}{R \left( \frac{\partial v}{\partial r} \right)_e} \right)^2 \quad (4)$$

where there appears an additional non-dimensional parameter

$$\Pi_4 = \frac{R(\partial v/\partial r)_e}{u_e} \quad (5)$$

which is also obtained from the LTE flow simulation in the ICP facility. The validity of Homann's correlation (3) for a cooled pitot probe in high enthalpy flows has been investigated in a separate study (next section).

The boundary layer edge enthalpy  $h_e$  and velocity gradient  $(\frac{\partial v}{\partial r})_e$  can then be reconstructed by solving the system

$$q_{w,\text{aux}} = BL(p_e, h_e, (\frac{\partial v}{\partial r})_e, \Pi_1, \Pi_2, \gamma_w = 1, T_{w,\text{aux}}) \quad (6)$$

$$\Delta p = \frac{K_p}{2\Pi_4^2} \rho_e(p_e, h_e) \left( R(\frac{\partial v}{\partial r})_e \right)^2 \quad (7)$$

in which  $q_{w,\text{aux}}$ ,  $T_{w,\text{aux}}$ ,  $p_e$  and  $\Delta p$  are known from experiments, and the non-dimensional parameters  $\Pi_i$  from the LTE simulation. This reconstruction process can be viewed again as a calibration of the stagnation line flow computational model.

Once the boundary layer edge properties have been determined, then the one-dimensional stagnation line flow solver can be run for various wall catalytic activity/temperature combinations to produce a heat flux abacus (set of  $q_w, T_w$  curves at constant catalytic activity  $\gamma_w$ ).

The catalytic activity of the TPS material of interest, for which the wall heat flux  $q_w$  and the wall temperature  $T_w$  have been measured, is then obtained graphically by identifying the  $\gamma_w$  contour on which the data point  $(q_w, T_w)$  lies, or alternatively by solving numerically Eqn. 2 for  $\gamma_w$ , all other quantities being known.

The procedure is now illustrated by a sample application in the VKI Plasmatron. The first step is the LTE viscous flow computation of the axially injected (no swirl) air flow in the facility with the following operational conditions:  $p = 10$  kPa,  $P = 75$  kW,  $q_m = 8$  gs<sup>-1</sup>. The computed temperature field is shown in Fig. 20 and the computed non-dimensional parameters are respectively

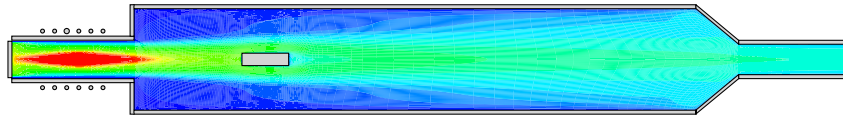
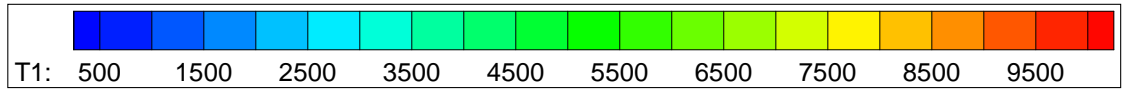


Figure 20: Computed temperature field in VKI Plasmatron facility

$\Pi_1 = 0.372$ ,  $\Pi_2 = 2.895$ ,  $\Pi_4 = 0.496$ . It is recalled that, as the non-dimensional parameters are (almost) independent of the pressure level and of the injected power, only the mass flow and the inlet flow swirl angle need to match between LTE viscous flow computation and experiment for the reconstruction procedure to be valid. Then, experimental measurements of the pitot pressure in the jet and of the heat flux to a cooled copper probe were performed under the following

operating conditions:  $q_m = 8 \text{ gs}^{-1}$ ,  $p = 2.5 \text{ kPa}$ ,  $P_{el} = 100 \text{ kW}$ , where  $P_{el}$  is the electrical power supplied by the HF generator. The results were:  $p_{\text{pitot}} - p_{\text{ref}} = 25 \text{ Pa}$ ,  $q_w = 547.5 \text{ kW m}^{-2}$ .

From these computational and experimental data, and the value of the pitot pressure recovery ratio taken to be  $K_p = 1.1$ , the boundary layer edge properties are reconstructed to be  $h_e = 13.85 \text{ MJ kg}^{-1}$  and  $(\partial v / \partial r)_e = 3710 \text{ s}^{-1}$ . These values are then used to construct a heat flux abacus as a function of the TPS material sample wall temperature and catalytic activity, shown in Fig. 21. Both the reconstruction and the heat flux abacus calculations were performed using

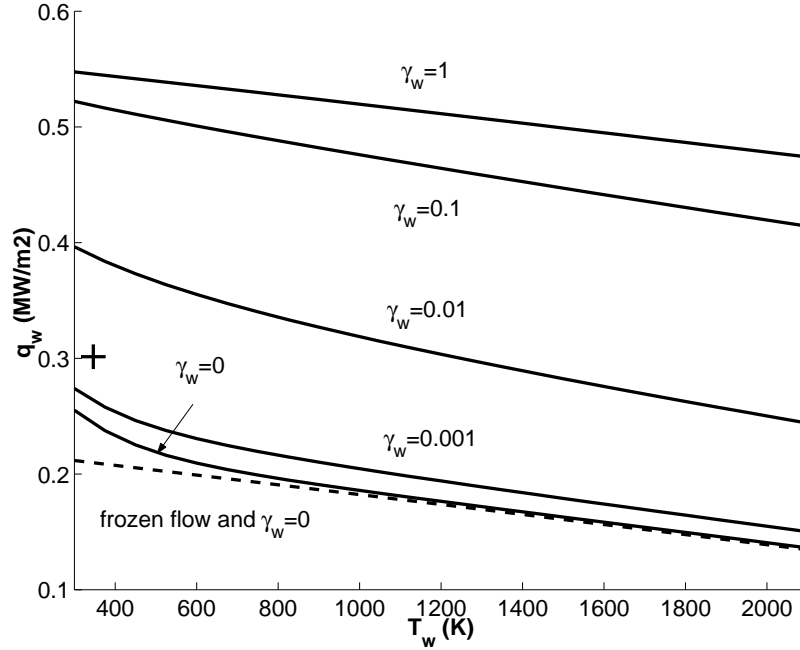


Figure 21: Heat flux abacus for VKI Plasmatron with air,  $q_m = 8 \text{ gs}^{-1}$ ,  $p = 2.5 \text{ kPa}$ ,  $P_{el} = 100 \text{ kW}$

the chemical kinetics model of Gupta [18]. The sensitivity of the method to the chemical kinetics model is presently being studied by A. García [19].

Finally, the heat flux to a quartz sample and its wall temperature were measured to deduce the catalytic activity of quartz in the VKI Plasmatron operating conditions. The experimental data point ( $q_w = 301.4 \text{ kW m}^{-2}$ ,  $T_w = 346.4 \text{ K}$ ) is shown on the heat flux abacus by the symbol +. The corresponding catalytic recombination probability was obtained by numerically solving Eqn. 2, providing the result  $\gamma_w = 3 \cdot 10^{-3}$ .

### Numerical study of the flow around a cooled pitot probe

The methodology to determine the catalytic activity of a TPS material sample in a hot plasma jet outlined in the previous section relies on a pitot pressure measurement to reconstruct the boundary layer edge properties. Whereas the meaning of a pitot pressure measurement in a high Reynolds number cold flow is well known ( $\Delta p = p_t - p$ ), it is far from being clear for a cooled pressure probe in a hot plasma jet. This question was therefore thoroughly investigated [20] by numerical simulations.

Defining  $\Delta p$  as the difference between the pressure at the stagnation point of the pitot probe (pitot pressure) and the local static pressure at the same location *in the absence of probe* ( $\Delta p = p_{\text{pitot}} - p$ ), this quantity was calculated from two LTE viscous flow computations, with probe and without probe, for various probe dimensions/wall temperatures to investigate Reynolds number and heat transfer effects. The essential conclusions of the investigation were the following:

- The pitot pressure increases very slightly with a decreasing probe wall temperature.
- The pitot pressure increases with decreasing probe dimensions, due to the well-known low-Reynolds number (Barker) effect.
- The pitot probe pressure recovery ratio defined as

$$K \equiv \frac{\Delta p}{p_t - p} \quad (8)$$

where  $p_t$  is the local total pressure (pressure that would be obtained from an isentropic deceleration to rest) calculated from the computation without probe, was found in good agreement with Homann's correlation [17] independently of the wall temperature, whose effect has been said to be small, and of the inlet flow swirl angle, showing that these parameters only have a minor influence on the pitot measurements.

- For the VKI ICP facilities flow conditions, it was shown that, because of the low flow Mach number and despite the complexity of thermodynamic equations of state due to the high temperatures, the Bernoulli formula is valid, viz.  $p_t - p \approx \rho u^2/2$ , so that

$$K \approx \frac{\Delta p}{\rho u^2/2} \equiv K_p$$

Actually of course, one doesn't measure  $\Delta p$  but rather the difference between the pitot pressure and a reference pressure somewhere in the flow (e.g. at a static pressure port on the test chamber wall or on the probe itself). Now, because the static pressure field in the plasma jet strongly depends on the inlet flow swirl angle, the non-dimensional coefficient

$$K_r = \frac{p_{\text{pitot}} - p_{\text{ref}}}{p_t - p} \quad (9)$$

also strongly depends on the inlet flow swirl angle. Whereas for an axial injection  $K_r$  is very close to  $K$  (because  $p_{\text{ref}} \approx p$ ), this is no longer true for swirling injection, the difference between  $K_r$  and  $K$  reaching 45% for the large cold wall probe. An important consequence is that the use of Eqn. 7 based on Homann's correlation for the reconstruction of the boundary layer edge properties is valid only for axial injection. For swirling injection, it is absolutely essential to reconstruct boundary layer edge properties using a value of  $K_r$  provided by the LTE viscous flow calculation of the flow around the probe, or equivalently to use  $\Pi_3 \equiv K_r/2\Pi_4^2$ .

## Conclusions

Examples of combined CFD and experimental studies carried out in the Aerospace department at the von Karman Institute over the past few years have been presented. The main lessons learned from these studies are the following.

In the hypersonic flow over a blunted cone/flare validation study, the importance of a careful model alignment to ensure flow axisymmetry has been demonstrated. The investigation of discrepancies in computed and measured surface heat fluxes revealed that they were due to incorrect computational inflow conditions, related to freestream non-uniformities.

The methodology to determine wall catalytic activity in a hot plasma jet constitutes a nice example of how computational simulations and experiments can help each other in cases where measurements are difficult to perform, and some computational simulation parameters are unknown.

Finally, the computational investigation of the flow around a cooled pitot probe in a hot plasma jet illustrated how computational simulation can help in the interpretation of experimental measurements, and in providing guidelines for data reduction.

#### *Acknowledgements*

The code validation study was directed by Prof. J.-M. Charbonnier, presently at CNES, and the experimental part was carried out by H. L. Boerrigter. The high enthalpy flow studies were partially supported by the INTAS Research Grant RFBR-95-1329 and benefited from fruitful discussions with Project Coordinator Dr. G. S. R. Sarma (DLR, Germany) and Project partner Dr. A. F. Kolesnikov (Institute for Problems in Mechanics, Moscow). A large part of the illustrative application was carried out by the VKI Diploma Course member A. García, under the supervision of Prof. O. Chazot.

## References

- [1] Verification and validation of computational fluid dynamics. von Karman Institute LS 2000-08, 2000.
- [2] F. Grasso, J. Périaux, and J.-A. Désidéri. The FLOWNet project: a flow library on the web. VKI LS 2000-08, 2000. See also <http://dataserv.inria.fr/flownet/index.php3>.
- [3] AIAA. Guide for the verification and validation of computational fluid dynamics. Guide AIAA-G-077-1998, American Institute of Aeronautics and Astronautics, Reston, Virginia, 1998.
- [4] W. Dieudonné, H. L. Boerrigter, and J.-M. Charbonnier. Hypersonic flow on a blunted cone-flare in the VKI H3 wind tunnel. Technical Note 193, von Karman Institute, 1997.
- [5] W. L. Oberkampf. Design, execution, and analysis of validation experiments. VKI LS 2000-08, 2000.
- [6] C. Mensink and H. Deconinck. A 2D parallel multiblock Navier-Stokes solver with applications on shared and distributed memory machines. First European Computational Fluid Dynamics Conference, Brussels, September 7-11 1992.
- [7] R. Broglia, M. Manna, H. Deconinck, and G. Degrez. Development and validation of an axisymmetric Navier-Stokes solver for hypersonic flows. Technical Note 188, von Karman Institute, 1995.
- [8] F. Coquel and M.-S. Liou. Field by field hybrid upwind splitting methods. AIAA Paper 93-3302 CP.
- [9] H. L. Boerrigter. Calibration of the H3 wind tunnel using Pitot probes. Internal Note 94, von Karman Institute, 1993.
- [10] P. R. Spalart and S. R. Allmaras. A one-equation turbulence model for aerodynamic flows. *La Recherche Aérospatiale*, (1):5–21, 1994.
- [11] A. F. Kolesnikov, I. S. Pershin, S. A. Vasil'evskii, and M. I. Yakushin. Study of quartz surface catalyticity in dissociated carbon dioxide subsonic flows. AIAA Paper 98-2847, 1998.

- [12] A. F. Kolesnikov. Combined measurements and computations of high enthalpy and plasma flows for determination of TPM surface catalycity. In J. M. Charbonnier and G. S. R. Sarma, editors, *Measurement Techniques for High Temperature and Plasma Flows*. NATO-RTO-EN 8, 1999.
- [13] P. F. Barbante. *Accurate and efficient modelling of high temperature non-equilibrium air flows*. PhD thesis, Université Libre de Bruxelles, 2001.
- [14] P. F. Barbante, G. Degrez, and G. S. R. Sarma. Computation of non-equilibrium high temperature axisymmetric boundary layer flows. *Journal of Thermophysics and Heat Transfer*, 16(4):490–497, 2002.
- [15] D. Vanden Abeele and G. Degrez. Efficient computational model for inductive plasma flows. *AIAA Journal*, 38(2):234–242, 2000.
- [16] T. Magin, D. Vanden Abeele, and G. Degrez. An implicit multiblock solver for inductive plasma flows. AIAA Paper 2000-2480.
- [17] F. Homann. The effect of high viscosity on the flow around a cylinder and around a sphere. Technical Memorandum TM-1334, NACA, 1952.
- [18] R. N. Gupta, J. M. Yos, R. A. Thompson, and K. P. Lee. A review of reaction rates and thermodynamic and transport properties for an 11-species air model for chemical and thermal nonequilibrium calculations to 30000 K. RP 1232, NASA, 1990.
- [19] A. García Muñoz. Catalycity effects in plasma flows. VKI Project Report 2001-12, 2001.
- [20] T. Magin and G. Degrez. Cooled pitot probe in inductive air plasma jet: what do we measure? Paper presented at the 2nd International Symposium on Atmospheric Reentry Vehicles and Systems, Arcachon, France, March 2001.